

# In-situ synchronous photoelectrosynthesis of H<sub>2</sub>O<sub>2</sub>/HClO green disinfectant with a S-scheme heterojunction bifunctional In<sub>2</sub>S<sub>3</sub>/MnIn<sub>2</sub>S<sub>4</sub> photoelectrocatalyst

Yaoyue Chen, Lei Zhang \*

College of Chemistry, Liaoning University, 66 Chongshan Middle Road, Shenyang, Liaoning 110036, People's Republic of China



## ARTICLE INFO

### Keywords:

Bifunctional hollow nanotube  
In-situ H<sub>2</sub>O<sub>2</sub> and HClO production  
Anode oxidation coupled with cathode reduction  
Synergistic degradation effect

## ABSTRACT

Photoelectrosynthesis of H<sub>2</sub>O<sub>2</sub>/HClO green disinfectant have great potential, but developing effective catalysts remains a significant challenge. We develop a hollow tube In<sub>2</sub>S<sub>3</sub>/MnIn<sub>2</sub>S<sub>4</sub> S-scheme bifunctional catalyst using ion exchange that can drive O<sub>2</sub> reduction reaction (ORR) on hydrophobic In<sub>2</sub>S<sub>3</sub>/MnIn<sub>2</sub>S<sub>4</sub>/PVDF/NF photocathode and Cl<sup>-</sup> oxidation reaction (ClOR) on hydrophilic In<sub>2</sub>S<sub>3</sub>/MnIn<sub>2</sub>S<sub>4</sub>/CP photoanode, accumulating practically useful concentrations of H<sub>2</sub>O<sub>2</sub>/HClO up to 2108 μmol·L<sup>-1</sup>/28.5 mg·L<sup>-1</sup>, respectively. With a two-electrode O<sub>2</sub>/Cl<sup>-</sup> co-photoelectrocatalysis system, H<sub>2</sub>O<sub>2</sub> and HClO can be simultaneously generated in H-type cell with a lower voltage by replacing OER with ClOR. In single-chamber cell, the activation of co-produced H<sub>2</sub>O<sub>2</sub> and HClO at electrode could generate <sup>1</sup>O<sub>2</sub> and more ·OH synergistically to degrade organic pollutants efficiently. This work provides a win-win strategy for simultaneous production of H<sub>2</sub>O<sub>2</sub> and HClO, efficient pollutant degradation for environmental and energy engineering.

## 1. Introduction

Hydrogen peroxide (H<sub>2</sub>O<sub>2</sub>) and hypochlorous acid (HClO) are commonly used worldwide for the organic synthesis, cleaning, textile bleaching, food sterilization and dye wastewater treatment because of their strong oxidation power in aqueous solutions [1,2]. The traditional ways to produce commercial H<sub>2</sub>O<sub>2</sub> and HClO rely on energy and waste-intensive anthraquinone [3] and chloralkali electrolysis [4] processes, respectively. The in-situ generation of H<sub>2</sub>O<sub>2</sub> and HClO through photocatalytic or photoelectrocatalytic process has the advantages of green safety and a ready-to-use nature [5]. By more sustainable, greener, and less energy-intensive photocatalytic or photoelectrocatalytic to produce H<sub>2</sub>O<sub>2</sub>/HClO is widely concerned. Traditionally, coupling the cathodic ORR with the anodic 4e<sup>-</sup> oxygen evolution reaction (OER) actually "wastes" most of the power input [6,7], greatly reducing economic benefits and sustainability due to the high potential barrier of anodic OER (1.23 V vs. RHE) and slow multiple proton-coupled electron-transfer kinetics [8,9]. Replacing the OER with suitable lower potential anodic oxidation reactions provides an innovative solution to this problem [10]. The combination of photoelectrocatalytic ORR and ClOR may effectively reduce the energy consumption and produce extra economic and environmental benefits, which still needs to be explored.

Ideally, integrating the advantages of ORR and ClOR catalysts to design and construct efficient ORR-ClOR bifunctional catalysts would be a promising strategy, which not only improves the efficiency of the system but also simplifies synthesis process.

It is well known that the design of photoelectrocatalysts is the most critical part of solar- and electro-driven ORR/ClOR. Metal sulfides such as In<sub>2</sub>S<sub>3</sub>, ZnIn<sub>2</sub>S<sub>4</sub> and CdIn<sub>2</sub>S<sub>4</sub> are intriguing visible light active catalysts with unique electronic structure, tunable optical properties, and suitable band gaps and band edges [11–13]. Some studies have been undertaken on regulating catalytic activity of In<sub>2</sub>S<sub>3</sub>, such as heterojunction interface tuning [14], defect engineering [15], structure and atomic doping [16]. Regrettably, such materials usually suffer sluggish interface transport kinetics (gas/ion) in practical research, leading to insufficient catalytic performance. It is important to effectively enhance the interface reaction kinetics of photoelectrode materials in order to overcome this problem. Until now, several interface and morphology engineering strategies have been proposed, including construction a novel step-scheme (S-scheme) heterojunction [17], Z-scheme heterojunction, [18], and morphology control resulting in different morphologies such as sphere-, sheet-, rod-, cube- and flower-like structures and so on [19]. Besides, the catalysts can be precisely modified by adjusting the wettability through stearic acid (SA), polytetrafluoroethylene (PTFE), poly(vinylidene fluoride)

\* Corresponding author.

E-mail address: [zhanglei63@126.com](mailto:zhanglei63@126.com) (L. Zhang).

(PVDF), polydimethylsiloxane (PDMS) to accelerate O<sub>2</sub> transmission and activation at the newly formed interfaces for the purpose of increasing the availability of O<sub>2</sub> and yield of H<sub>2</sub>O<sub>2</sub> [20–23].

Inspired by the above considerations, a hollow tubular bifunctional S-scheme heterojunction In<sub>2</sub>S<sub>3</sub>/MnIn<sub>2</sub>S<sub>4</sub> photoelectrocatalyst was synthesized for the first time through ion exchange method for better light absorption, photogenerated carrier transport and separation, and catalytic performance, achieving simultaneously superior activity for the ORR and ClOR. The proposed dual-functional material strategy would simplify the catalytic electrode fabrication to avoid the separate synthesis of two electrode materials and reduce the overall cost. To further accelerate O<sub>2</sub> mass transfer, In<sub>2</sub>S<sub>3</sub>/MnIn<sub>2</sub>S<sub>4</sub>/PVDF/NF photocathode was fabricated by coating In<sub>2</sub>S<sub>3</sub>/MnIn<sub>2</sub>S<sub>4</sub> catalytic layer on hydrophobic porous PVDF-modified Ni foam (PVDF/NF) to produce high yield of H<sub>2</sub>O<sub>2</sub> (2108 μmol/L). In<sub>2</sub>S<sub>3</sub>/MnIn<sub>2</sub>S<sub>4</sub>/CP photoanode was fabricated by dropping In<sub>2</sub>S<sub>3</sub>/MnIn<sub>2</sub>S<sub>4</sub> onto carbon paper (CP), which had a stronger oxidation activity toward Cl<sup>-</sup> to generate a relatively high concentration of HClO (28.5 mg/L). For win-win goals, coupling cathodic ORR with anodic ClOR to realize H<sub>2</sub>O<sub>2</sub> and HClO production simultaneously. Combining the ORR and ClOR can utilize the synergistic effect of the in-situ generated H<sub>2</sub>O<sub>2</sub> and HClO to generate <sup>1</sup>O<sub>2</sub> and more ·OH by activating HClO and H<sub>2</sub>O<sub>2</sub> at electrode, achieving high-efficiency degradation of organic pollutants. This work is expected to pave the way for designing of bifunctional photoelectrocatalysts for efficient co-production of H<sub>2</sub>O<sub>2</sub> and HClO, and propose a new mechanism for enhanced contaminant degradation under H<sub>2</sub>O<sub>2</sub>-HClO coupling mode.

## 2. Experimental section

### 2.1. Catalysts synthesis

#### 2.1.1. Synthesis of MIL-68(In)

Typically, 60 mg of In(NO<sub>3</sub>)<sub>3</sub>·xH<sub>2</sub>O and 60 mg of H<sub>2</sub>BDC were dissolved in 40 mL of DMF, and stirred until a clear solution was formed. After that, the mixture was heated to 120 °C in an oil bath for 30 min. The white precipitate was filtrated and washed with ethanol, and then dried at 80 °C in vacuum.

#### 2.1.2. Synthesis of MOF-derived In<sub>2</sub>S<sub>3</sub>

For synthesis of In<sub>2</sub>S<sub>3</sub> nanotubes derived from In-MOF, 0.1 g of the obtained MIL-68(In) precursors were added into 15 mL of ethanol solution containing 0.3 g of CH<sub>4</sub>N<sub>2</sub>S, and stirred for 10 min. Then, the mixture was transferred into a 100 mL Teflon-lined autoclave and maintained at 180 °C for 24 h. After cooling down, the yellow precipitate was filtrated and washed with ethanol three times, and dried at 60 °C in vacuum.

#### 2.1.3. Synthesis of In<sub>2</sub>S<sub>3</sub>/MnIn<sub>2</sub>S<sub>4</sub> and MnIn<sub>2</sub>S<sub>4</sub>

Generally, 30 mg of In<sub>2</sub>S<sub>3</sub> was well dispersed in 20 mL of ethanol under continuous stirring treatment, and then, into which 5 mL of Mn<sup>2+</sup> ethanol solution with certain concentrations was quickly added. After stirring at 60 °C for 2 h, the resulting mixture was filtered, washed with ethanol and DI water, and dried at 60 °C under vacuum. The samples obtained after the ion exchange reaction for different amounts of Mn<sup>2+</sup> were designated as In<sub>2</sub>S<sub>3</sub>/MnIn<sub>2</sub>S<sub>4</sub>-5, In<sub>2</sub>S<sub>3</sub>/MnIn<sub>2</sub>S<sub>4</sub>-10 and In<sub>2</sub>S<sub>3</sub>/MnIn<sub>2</sub>S<sub>4</sub>-15, where the suffix indicates the weight ratio of In<sub>2</sub>S<sub>3</sub> in the hybrid. MnIn<sub>2</sub>S<sub>4</sub> was prepared with excess Mn<sup>2+</sup> exchange under same conditions.

## 2.2. Electrode Synthesis and Modification

### 2.2.1. Synthesis of In<sub>2</sub>S<sub>3</sub>/MnIn<sub>2</sub>S<sub>4</sub>/PVDF/NF photocathode

Ni foam (NF, 2 cm × 3 cm × 2 mm) needed to be firstly cleaned remove oil and oxide from the surface. The cleaned NF was soaked in PVDF suspension (3 mg/mL) for 10 min and then calcined at 240 °C for 30 min to prepare PVDF/NF. The In<sub>2</sub>S<sub>3</sub>/MnIn<sub>2</sub>S<sub>4</sub> was immobilized on

PVDF/NF, 5 mg of In<sub>2</sub>S<sub>3</sub>/MnIn<sub>2</sub>S<sub>4</sub> was ultrasonically dispersed in 1 mL of DMF, then was coated on PVDF/NF to form a catalytic layer. In<sub>2</sub>S<sub>3</sub>/MnIn<sub>2</sub>S<sub>4</sub>/PVDF/NF was obtained by immobilization at 120 °C for 30 min. In<sub>2</sub>S<sub>3</sub>/MnIn<sub>2</sub>S<sub>4</sub>/NF was also obtained without PVDF treatment as the control group.

### 2.2.2. Synthesis of In<sub>2</sub>S<sub>3</sub>/MnIn<sub>2</sub>S<sub>4</sub>/CP photoanode

The photoanode was prepared by dispersing 3 mg of catalyst into 400 μL of deionized water and 1.5 μL of Nafion solution, followed by ultrasonic treatment for 30 min. Then the catalysts ink was loaded onto carbon paper (CP) and dried naturally.

### 2.3. PEC H<sub>2</sub>O<sub>2</sub> production by the In<sub>2</sub>S<sub>3</sub>/MnIn<sub>2</sub>S<sub>4</sub>/PVDF/NF photocathode

The cathodic H<sub>2</sub>O<sub>2</sub> productivity was investigated in a three-electrode configuration by using an Ag/AgCl reference electrode and a Pt counter electrode, respectively. The reaction was carried out in 20 mL of 0.1 M Na<sub>2</sub>SO<sub>4</sub> solution (containing 2 mL of EtOH, pH = 3 with 0.5 mol/L HClO<sub>4</sub>) with a rotating speed of 150 rpm under visible light irradiation ( $\lambda > 420$  nm) with a 300 W Xenon lamp, the In<sub>2</sub>S<sub>3</sub>/MnIn<sub>2</sub>S<sub>4</sub>/PVDF/NF worked as cathode. The concentration of H<sub>2</sub>O<sub>2</sub> was determined by potassium titanium oxalate method and the absorbance was determined by UV-vis spectrometry (standard curve was shown in Fig. S1).

### 2.4. PEC HClO production by the In<sub>2</sub>S<sub>3</sub>/MnIn<sub>2</sub>S<sub>4</sub>/CP photoanode

The cathodic H<sub>2</sub>O<sub>2</sub> productivity was investigated in a three-electrode configuration by using an Ag/AgCl reference electrode and a Pt counter electrode, respectively. The reaction was carried out in 20 mL of 35 g/L NaCl solution with a rotating speed of 150 rpm, in which Pt plate was used as cathode, the In<sub>2</sub>S<sub>3</sub>/MnIn<sub>2</sub>S<sub>4</sub>/CP worked as anode. The generated HClO in solution was analyzed using DPD (N,Ndiethyl-p phenylenediamine) reagents by UV-vis spectrophotometry method (standard curve was shown in Fig. S2).

### 2.5. PEC H<sub>2</sub>O<sub>2</sub>-HClO production by photocathode-anode coupling

In<sub>2</sub>S<sub>3</sub>/MnIn<sub>2</sub>S<sub>4</sub>/PVDF/NF as photocathode and In<sub>2</sub>S<sub>3</sub>/MnIn<sub>2</sub>S<sub>4</sub>/CP as photoanode to form photochemical cell to produce H<sub>2</sub>O<sub>2</sub> and HClO. The H-type cell exploited Nafion membrane as a separator, with 0.1 mol/L Na<sub>2</sub>SO<sub>4</sub> solution and 35 g/L NaCl solution as the catholyte and anolyte, respectively. The detection methods of H<sub>2</sub>O<sub>2</sub> and HClO were the same as those mentioned previously.

### 2.6. In-situ Fenton degradation of H<sub>2</sub>O<sub>2</sub>, HClO and HClO-H<sub>2</sub>O<sub>2</sub> coupling systems

A different group of control experiments were performed to systematically investigate the synergistic effect of H<sub>2</sub>O<sub>2</sub> and HClO activation into ·OH for enhanced Fenton degradation of methylene blue (MB). In a single-chamber cell with a 20 mL working volume, containing 0.1 mol/L Na<sub>2</sub>SO<sub>4</sub> and 35 g/L NaCl was used as the electrolyte with 10 mg/L of MB. The In<sub>2</sub>S<sub>3</sub>/MnIn<sub>2</sub>S<sub>4</sub>/PVDF/NF cathode, with the In<sub>2</sub>S<sub>3</sub>/MnIn<sub>2</sub>S<sub>4</sub>/CP anode and Ag/AgCl as reference electrode, were used. O<sub>2</sub> was constantly provided.

### 2.7. Method of concentrating H<sub>2</sub>O<sub>2</sub>

The high concentration H<sub>2</sub>O<sub>2</sub> solution was obtained using different saturated vapor pressures of H<sub>2</sub>O and H<sub>2</sub>O<sub>2</sub>. Firstly, 19.5 mL of H<sub>2</sub>O<sub>2</sub> solution was put in a conical flask and the flask was sealed with a filter paper. The obtained low concentration H<sub>2</sub>O<sub>2</sub> solution (tap water as the electrolyte) was placed in a vacuum oven for 56 h at 30 °C, and 19.5 mL of low concentration H<sub>2</sub>O<sub>2</sub> solution was concentrated into 5.5 mL of high concentration H<sub>2</sub>O<sub>2</sub> solution.

### 3. Results and discussion

#### 3.1. Hydrophilic / Hydrophobic photocathode synthesis and modification

##### 3.1.1. Hydrophilic photocathode materials

The  $\text{In}_2\text{S}_3/\text{MnIn}_2\text{S}_4$  materials were obtained by an ion exchange method, as illustrated in Fig. 1a. As shown in Fig. 1b, the synthesized MIL-68 (In) had an ideal regular solid hexagonal rod with the average length and diameter of 1.3–2.2  $\mu\text{m}$  and 1  $\mu\text{m}$ , respectively. After sulfidation treatment, the solid hexagonal rod-shaped In-MIL-68 was transformed into the hierarchical hollow open-end tubular  $\text{In}_2\text{S}_3$ , the randomly assembled ultrathin nanosheets were observed to closely attached on the surface (Fig. 1c). Then, the hollow open-end tubulars  $\text{In}_2\text{S}_3$  were changed into  $\text{In}_2\text{S}_3/\text{MnIn}_2\text{S}_4$  hybrids via an efficient cation exchange reaction with  $\text{Mn}^{2+}$  ions at 60 °C for 2 h. Interestingly, the morphology of  $\text{In}_2\text{S}_3/\text{MnIn}_2\text{S}_4$  after  $\text{Mn}^{2+}$  exchange treatment maintained the hierarchical hollow open-end tubulars structure, and the surface of the tubes wall became rougher and tighter (Fig. 1d), which enhanced the interfacial contact and increased the specific surface area. When excess  $\text{Mn}^{2+}$  was involved in the reaction, the morphology of the synthesized product  $\text{MnIn}_2\text{S}_4$  was almost the same as that of  $\text{In}_2\text{S}_3/\text{MnIn}_2\text{S}_4$  (Fig. 1e).

Besides, the TEM image further revealed the hollow structure of the nanotubes and the existence of nanosheets, which implied that the catalyst with a tailored nanostructure was constructed. Further HRTEM measurement indicated the formation of homogeneous interfacial contacts between  $\text{In}_2\text{S}_3$  and  $\text{MnIn}_2\text{S}_4$  (Fig. 1f). Two lattice stripes of 0.323 and 0.253 nm respectively were shown in Fig. 1g, which could correspond to the (311) plane of  $\text{MnIn}_2\text{S}_4$  and the (411) plane of  $\text{In}_2\text{S}_3$ . Furthermore, the EDS mapping spectra (Fig. 1h) indicated that the elements S, In and Mn were evenly distributed throughout the heterostructure, confirming the successful construction of a hollow  $\text{In}_2\text{S}_3/\text{MnIn}_2\text{S}_4$ .

$\text{MnIn}_2\text{S}_4$  heterojunction, which was consistent with the SEM-EDS results (Fig. S3).

The crystalline structure of the prepared photocatalysts was revealed in the XRD patterns. As shown in Fig. S4, all diffraction peaks of MIL-68 (In) matched well with the standard [24], indicating the successful preparation and high crystallinity of MIL-68(In) crystal. After the sulfidation treatment, the prominent peaks of MIL-68(In) completely disappeared, and converted into cubic  $\text{In}_2\text{S}_3$  phase (JCPDS NO. 32-0456) [25]. The diffraction peaks at 27.5°, 28.8°, 33.4°, 47.9°, 56.1° and 59.6° were corresponded to the (311), (222), (400), (440), (533) and (444). Undergoing complete cation exchange of  $\text{In}_2\text{S}_3$  sample by  $\text{Mn}^{2+}$ , the diffraction peaks of  $\text{MnIn}_2\text{S}_4$  at 27.6°, 33.4°, 47.9°, 56.2° and 59.7° were well corresponding to the (311), (400), (440), (533) and (444) planes of  $\text{MnIn}_2\text{S}_4$  (JCPDS No. 79-1014). Whereas the XRD diffraction peaks of the  $\text{In}_2\text{S}_3/\text{MnIn}_2\text{S}_4$  samples synthesized through the ion exchange method resembled those of  $\text{MnIn}_2\text{S}_4$  and  $\text{In}_2\text{S}_3$ , possibly due to the similar crystal structures.

XPS analyses were performed to obtain an insight of the elemental compositions and their chemical states in the samples. Obviously, the characteristic peaks at 444.63 eV and 452.22 eV were ascribed to the  $3d_{5/2}$  and  $3d_{3/2}$  orbitals of  $\text{In}^{3+}$  in  $\text{In}_2\text{S}_3/\text{MnIn}_2\text{S}_4$  [14,25] (Fig. 2a). The two binding energy peaks located at around 161.18 eV and 162.32 eV correspond to the  $2p_{3/2}$ ,  $2p_{1/2}$  orbitals of  $\text{S}^{2-}$  in  $\text{In}_2\text{S}_3/\text{MnIn}_2\text{S}_4$  [26,27] (Fig. 2b). Furthermore, the three peaks correspond to  $\text{Mn} 2p_{1/2}$  (655.5 eV),  $\text{Mn} 2p_{3/2}$  (641.6 and 642.2 eV) in the  $\text{Mn} 2p$  spectrum [28] (Fig. 2c), suggesting the existence of  $\text{Mn}^{2+}$  and  $\text{Mn}^{3+}$ . Noteworthily, the band peaks of  $\text{In} 3d$ ,  $\text{S} 2p$ ,  $\text{Mn} 2p$  in the case of  $\text{In}_2\text{S}_3/\text{MnIn}_2\text{S}_4$  composite contrast to that of  $\text{MnIn}_2\text{S}_4$  shift to a higher binding energy, indicating that  $\text{MnIn}_2\text{S}_4$  would lose electrons when being fabricated with  $\text{In}_2\text{S}_3$ . Correspondingly, the lower energy shifts for  $\text{In} 3d$ ,  $\text{S} 2p$  in  $\text{In}_2\text{S}_3/\text{MnIn}_2\text{S}_4$  against  $\text{In}_2\text{S}_3$  suggest the influx of electrons in  $\text{In}_2\text{S}_3$ . The charge migration from  $\text{MnIn}_2\text{S}_4$  to  $\text{In}_2\text{S}_3$  resulted in a depletion layer of

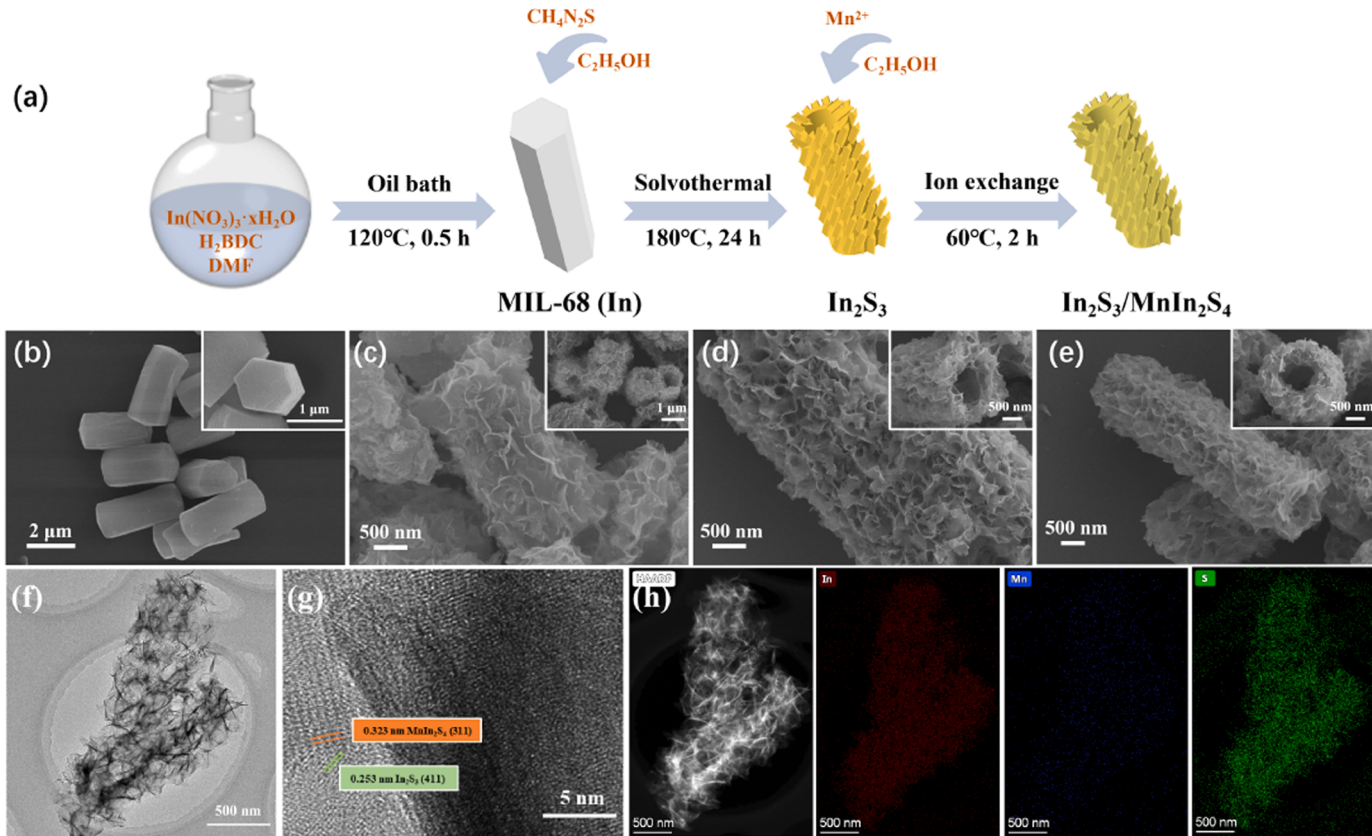


**Fig. 1.** (a) The illustration to prepare  $\text{In}_2\text{S}_3/\text{MnIn}_2\text{S}_4$  catalyst; SEM images of (b) MIL-68 (In); (c)  $\text{In}_2\text{S}_3$ ; (d)  $\text{In}_2\text{S}_3/\text{MnIn}_2\text{S}_4$ ; (e)  $\text{MnIn}_2\text{S}_4$ ; (f) TEM and (g) HRTEM images of  $\text{In}_2\text{S}_3/\text{MnIn}_2\text{S}_4$ ; (h) EDS elemental mapping of  $\text{In}_2\text{S}_3/\text{MnIn}_2\text{S}_4$ .

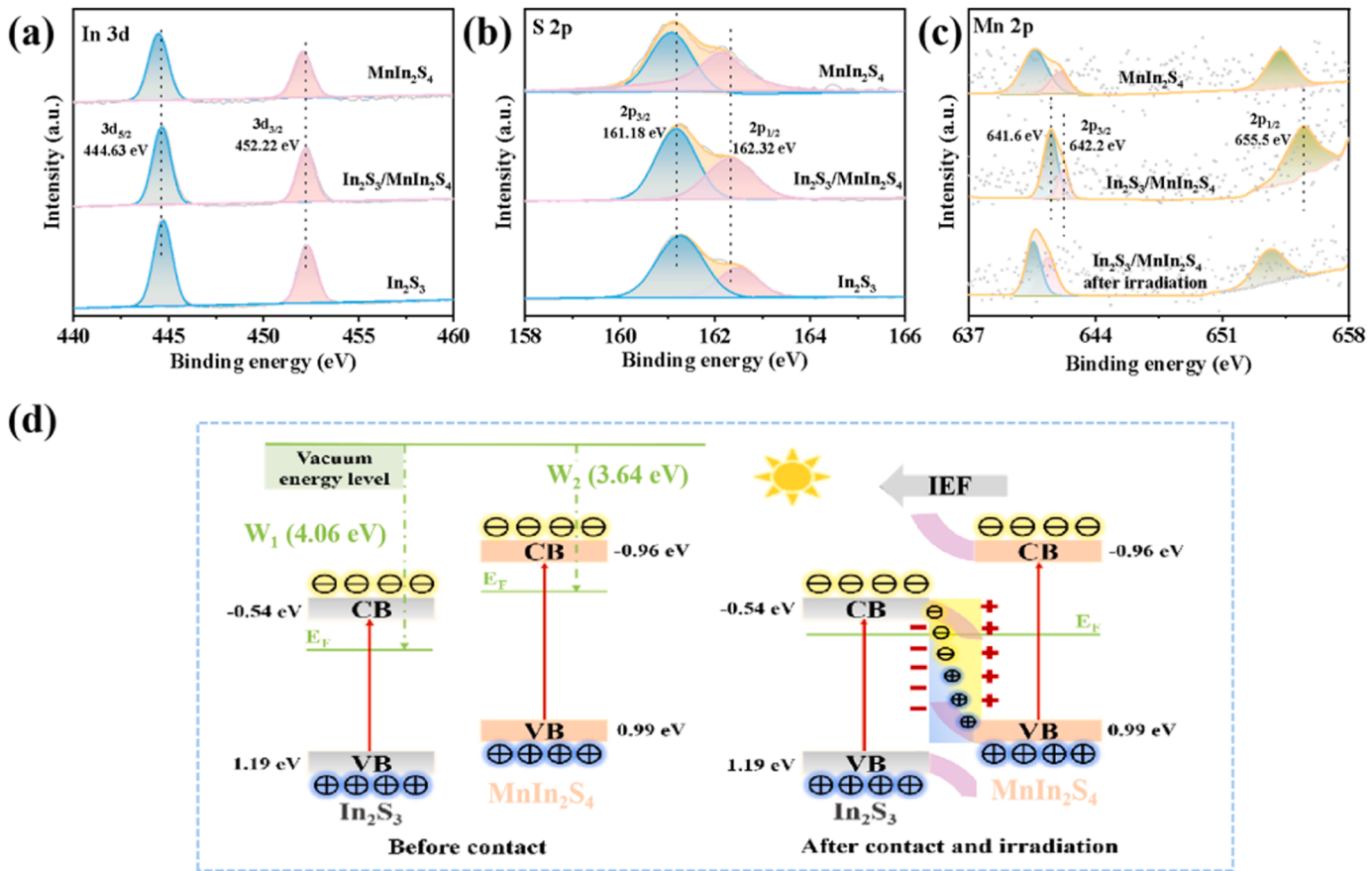


**Fig. 2.** (a-c) high-resolution XPS spectra of In 3d, S 2p and Mn 2p orbitals for In<sub>2</sub>S<sub>3</sub>, MnIn<sub>2</sub>S<sub>4</sub>, In<sub>2</sub>S<sub>3</sub>/MnIn<sub>2</sub>S<sub>4</sub> and In<sub>2</sub>S<sub>3</sub>/MnIn<sub>2</sub>S<sub>4</sub> after irradiation; (d) the S-scheme charge transfer mechanism between In<sub>2</sub>S<sub>3</sub> and MnIn<sub>2</sub>S<sub>4</sub>.

MnIn<sub>2</sub>S<sub>4</sub> and an accumulation layer of In<sub>2</sub>S<sub>3</sub> at the interface. Consequently, an internal electric field between the two layers in heterojunctions was built. Additionally, the reduced binding energy of Mn 2p in the irradiated In<sub>2</sub>S<sub>3</sub>/MnIn<sub>2</sub>S<sub>4</sub> compared to that without illumination, which indicated the photogenerated electron gaining of MnIn<sub>2</sub>S<sub>4</sub> from In<sub>2</sub>S<sub>3</sub> under the internal electric field (see Fig. 2c). These results may be consistent well with the characteristics of S-scheme photocatalyst (Fig. 2d) [29,30].

The UV-vis DRS displayed that In<sub>2</sub>S<sub>3</sub>/MnIn<sub>2</sub>S<sub>4</sub> harvest more light than In<sub>2</sub>S<sub>3</sub> and MnIn<sub>2</sub>S<sub>4</sub> (Fig. S5a). The band gap ( $E_g$ ) of In<sub>2</sub>S<sub>3</sub>, MnIn<sub>2</sub>S<sub>4</sub> and In<sub>2</sub>S<sub>3</sub>/MnIn<sub>2</sub>S<sub>4</sub> were 1.73 eV, 1.95 eV and 1.67 eV, respectively. Generally, the potential of normal hydrogen electrode (NHE) at 0 V is  $-4.5$  eV relative to the vacuum energy level ( $E_{VAC}$ ). According to the Mott-Schottky plots (Fig. S5b-c), the flat band ( $E_{FB}$ ) of In<sub>2</sub>S<sub>3</sub> and MnIn<sub>2</sub>S<sub>4</sub> are  $-0.44$  V vs. NHE and  $-0.86$  V vs. NHE. For n-type semiconductors, the  $E_{FB}$  is approximately the Fermi energy ( $E_F$ ), thus the work function ( $W$ ) obtained from  $W = E_{VAC} - E_F$  for In<sub>2</sub>S<sub>3</sub> and MnIn<sub>2</sub>S<sub>4</sub> are 4.06 eV and 3.64 eV, respectively. Because MnIn<sub>2</sub>S<sub>4</sub> exhibited a smaller work function than In<sub>2</sub>S<sub>3</sub>, when In<sub>2</sub>S<sub>3</sub> was in contact with MnIn<sub>2</sub>S<sub>4</sub>, the photoexcited electrons on MnIn<sub>2</sub>S<sub>4</sub> flowed to In<sub>2</sub>S<sub>3</sub>, and the energy bands of MnIn<sub>2</sub>S<sub>4</sub> and In<sub>2</sub>S<sub>3</sub> were bent upward and downward respectively. Thus, an internal electric field was formed at the heterojunction interface from MnIn<sub>2</sub>S<sub>4</sub> toward In<sub>2</sub>S<sub>3</sub>. In this way, the S-scheme heterojunction between In<sub>2</sub>S<sub>3</sub> and MnIn<sub>2</sub>S<sub>4</sub> was formed due to its suitable energy band structure and arrangement (Fig. 2d), which can maintain the maximum redox capacity of photogenerated charge carriers, well agreeing with the above XPS analysis. It can be confirmed by photocurrent, PL spectra and EIS that the prepared hollow heterojunctions prepared could efficiently facilitate interfacial charge transfer and simultaneously inhibit photo-excited electron-hole recombination (Fig. S5d-f).

### 3.1.2. Hydrophobic photocathode materials

The Ni foam (NF) was selected as the conductive substrate because of its highly developed porous structure and large specific surface area, allowing more molecular O<sub>2</sub> to contact the electrode. As shown in Fig. 3a, hydrophobic PVDF-modified NF (PVDF/NF) was firstly obtained, then In<sub>2</sub>S<sub>3</sub>/MnIn<sub>2</sub>S<sub>4</sub>/PVDF/NF hydrophobic electrode was prepared. The SEM images confirmed that In<sub>2</sub>S<sub>3</sub>/MnIn<sub>2</sub>S<sub>4</sub> were high-density and uniformly covered on PVDF modified skeleton of NF as the hydrophobic interface with a contact angle of 128.7° (Fig. 3b). In contrast, the In<sub>2</sub>S<sub>3</sub>/MnIn<sub>2</sub>S<sub>4</sub>/NF exhibited hydrophilic property with a water contact angle of approximately 0° (Fig. 3c). As shown in Fig. 3d, PVDF will slightly reduce the light absorption. To explore the intrinsic activities of the electrodes, the electrochemically active surface area (ECSA) was examined by cyclic voltammetry (CV) (Fig. S6). The charge transfer resistance ( $R_c$ ) of the electrodes was also determined. As shown in Fig. 3e-f, the lower ECSA and larger  $R_c$  of the In<sub>2</sub>S<sub>3</sub>/MnIn<sub>2</sub>S<sub>4</sub>/PVDF/NF electrode were ascribed to the reduced interfacial area between the solid catalytic surface and liquid electrolyte solution, supporting the idea of its increased triphase reaction interfaces.

### 3.2. *In situ* H<sub>2</sub>O<sub>2</sub> production on photocathode

The catalyst effect on H<sub>2</sub>O<sub>2</sub> production was firstly studied (Fig. S7). The In<sub>2</sub>S<sub>3</sub>/MnIn<sub>2</sub>S<sub>4</sub>/PVDF/NF and In<sub>2</sub>S<sub>3</sub>/MnIn<sub>2</sub>S<sub>4</sub>/NF electrodes were used in an O<sub>2</sub>-saturated Na<sub>2</sub>SO<sub>4</sub> solution to produce H<sub>2</sub>O<sub>2</sub> for evaluating the ORR performance (Fig. 4a and Fig. S8). The optimum PEC performance was achieved by In<sub>2</sub>S<sub>3</sub>/MnIn<sub>2</sub>S<sub>4</sub>/PVDF/NF (catalyst amount: 3 mg, pH=3) exposed to visible light for 1.5 h at  $-0.6$  V<sub>Ag/AgCl</sub>, the high-yield H<sub>2</sub>O<sub>2</sub> production of 2107.8 μmol/L was achieved, which is about 6-fold higher than that of In<sub>2</sub>S<sub>3</sub>/MnIn<sub>2</sub>S<sub>4</sub>/NF. The oxygen mass

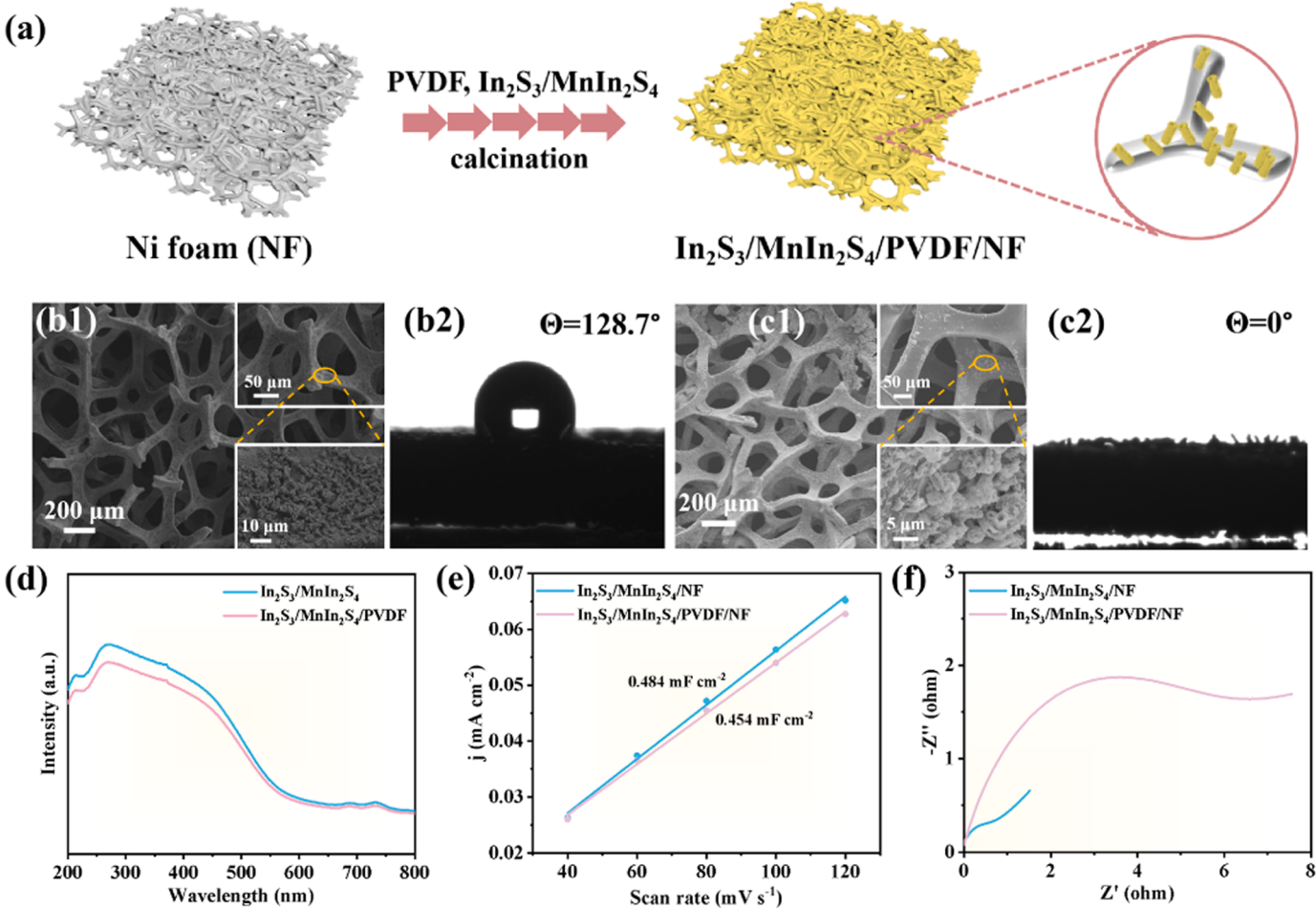


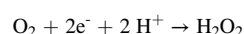
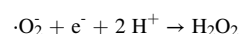
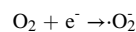
**Fig. 3.** (a) Preparation schematic illustration of  $\text{In}_2\text{S}_3/\text{MnIn}_2\text{S}_4/\text{PVDF}/\text{NF}$  electrode; (b-c) SEM images of  $\text{In}_2\text{S}_3/\text{MnIn}_2\text{S}_4/\text{PVDF}/\text{NF}$  and  $\text{In}_2\text{S}_3/\text{MnIn}_2\text{S}_4/\text{NF}$  and the corresponding water contact angle; (d) UV-vis DRS spectra of  $\text{In}_2\text{S}_3/\text{MnIn}_2\text{S}_4/\text{PVDF}/\text{NF}$  and  $\text{In}_2\text{S}_3/\text{MnIn}_2\text{S}_4/\text{NF}$ ; (e) double layer capacitance of  $\text{In}_2\text{S}_3/\text{MnIn}_2\text{S}_4/\text{PVDF}/\text{NF}$  and  $\text{In}_2\text{S}_3/\text{MnIn}_2\text{S}_4/\text{NF}$  for ECSA evaluation; (f) Nyquist plots of the  $\text{In}_2\text{S}_3/\text{MnIn}_2\text{S}_4/\text{PVDF}/\text{NF}$  and  $\text{In}_2\text{S}_3/\text{MnIn}_2\text{S}_4/\text{NF}$  electrodes.

transfer process is the crucial factor in affecting the reaction kinetics, therefore, ORR photocurrent tests of  $\text{In}_2\text{S}_3/\text{MnIn}_2\text{S}_4/\text{NF}$  and  $\text{In}_2\text{S}_3/\text{MnIn}_2\text{S}_4/\text{PVDF}/\text{NF}$  were performed at  $-0.6 \text{ V}_{\text{Ag}/\text{AgCl}}$ . As shown in Fig. 4b, for  $\text{In}_2\text{S}_3/\text{MnIn}_2\text{S}_4/\text{NF}$ , the photocurrent intensity gradually decreased sharply for each section of irradiation, demonstrating the gradually exhausted dissolved oxygen and a slow oxygen mass transfer process in the liquid phase.  $\text{In}_2\text{S}_3/\text{MnIn}_2\text{S}_4/\text{PVDF}/\text{NF}$  kept a photocurrent intensity without obvious decline, suggesting a higher local oxygen concentration and faster oxygen mass transfer at the hydrophobic tri-phase interface. The  $\text{H}_2\text{O}_2$  decomposition behavior also revealed that  $\text{In}_2\text{S}_3/\text{MnIn}_2\text{S}_4/\text{PVDF}/\text{NF}$  was available to inhibit the  $\text{H}_2\text{O}_2$  decomposition (Fig. 4c), which may be due to the presence of PVDF can prevent the adsorption of  $\text{H}_2\text{O}_2$  onto the  $\text{In}_2\text{S}_3/\text{MnIn}_2\text{S}_4$  surface owing to its hydrophobic character, thereby reducing the decomposition of  $\text{H}_2\text{O}_2$  [31]. The proposed enhancement mechanism of  $\text{H}_2\text{O}_2$  generation was shown in Fig. 4d.

In order to evaluate the stability and recyclability of  $\text{In}_2\text{S}_3/\text{MnIn}_2\text{S}_4/\text{PVDF}/\text{NF}$ , cycling test of PEC  $\text{H}_2\text{O}_2$  production was carried out (Fig. 4e), there was no significant reduction in production and FE (%) can be maintained at more than 50%, the  $\text{In}_2\text{S}_3/\text{MnIn}_2\text{S}_4/\text{PVDF}/\text{NF}$  still showed a hydrophobicity with a contact angle of  $120.5^\circ$ . To further demonstrate the excellent performance of  $\text{H}_2\text{O}_2$  production with photocathode. The  $\text{H}_2\text{O}_2$  produced by  $\text{In}_2\text{S}_3/\text{MnIn}_2\text{S}_4/\text{PVDF}/\text{NF}$  was compared with that of other reported electrodes materials, as shown in Fig. 4f. The results indicated that the  $\text{In}_2\text{S}_3/\text{MnIn}_2\text{S}_4/\text{PVDF}/\text{NF}$  photocathode had the highest PEC  $\text{H}_2\text{O}_2$  production among other reported

hydrophobic photoelectrodes, which was comparable to the electrocatalytic (EC)  $\text{H}_2\text{O}_2$  production of N-porous Carbon/CF [21,32–34].

To explore the PEC ORR pathway, free radical capture experiments were conducted to investigate active groups involved during the  $\text{H}_2\text{O}_2$  generation process. As observed in Fig. 5a, it indicated that  $\text{e}^-$  and  $\cdot\text{O}_2$  were the main active species involved in the ORR reaction due to the significant reduction in the  $\text{H}_2\text{O}_2$  production by adding potassium persulfate and p-benzoquinone. The presence of ammonium oxalate could continuously consume  $\text{h}^+$  and leaving more  $\text{e}^-$  for the ORR reaction to produce  $\text{H}_2\text{O}_2$ . Besides, the production of  $\text{H}_2\text{O}_2$  was reduced obviously with furfuryl alcohol, indicating that  $\cdot\text{O}_2$  also played a role in  $\text{H}_2\text{O}_2$  generation. The  $\text{H}_2\text{O}_2$  produced was completely inhibited in  $\text{N}_2$  atmosphere, which also showed the importance of  $\text{O}_2$  in the ORR reaction. The addition of isopropyl alcohol inhibited the formation of hydrogen peroxide, indicating the existence of  $\cdot\text{OH}$ , possibly from the decomposition of  $\text{H}_2\text{O}_2$ . The EPR spin-trapping experiments were further performed, the DMPO- $\cdot\text{O}_2$ , DMPO- $\cdot\text{OH}$  and TEMP- $\cdot\text{O}_2$  signals were identified (Fig. 5b). The average number of transferred electrons ( $n$ ) of  $\text{In}_2\text{S}_3/\text{MnIn}_2\text{S}_4$  in ORR was calculated to be 2.08 from Koutecky-levich plot data of a rotating circular disk electrode (Fig. S9 and Fig. 5c). In summary, it is believed that the single-electron and two-electron reduction pathway for  $\text{H}_2\text{O}_2$  generation:



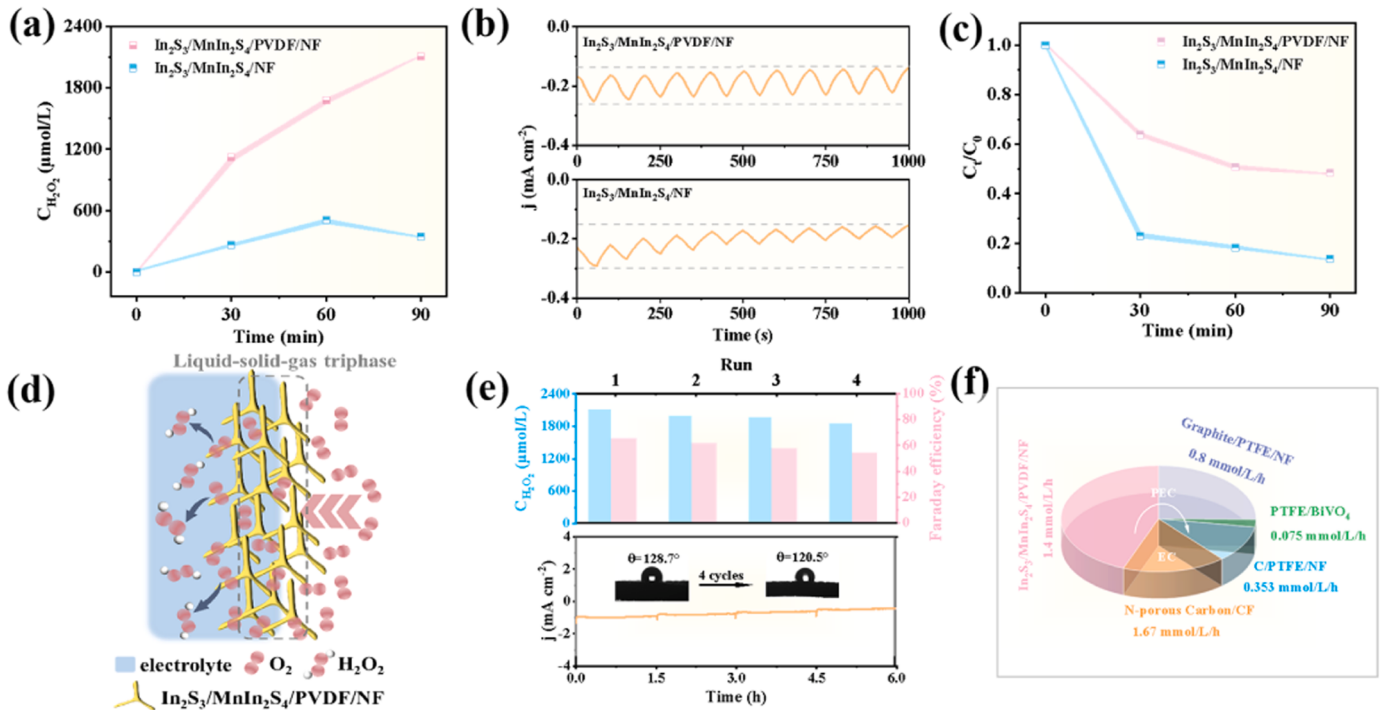


**Fig. 4.** (a) PEC  $\text{H}_2\text{O}_2$  production; (b) oxygen reduction photocurrent curves of  $\text{In}_2\text{S}_3/\text{MnIn}_2\text{S}_4/\text{PVDF/NF}$  and  $\text{In}_2\text{S}_3/\text{MnIn}_2\text{S}_4/\text{NF}$  at  $-0.6 \text{ V}_{\text{Ag}/\text{AgCl}}$ ; (c) PEC  $\text{H}_2\text{O}_2$  decomposition of  $\text{In}_2\text{S}_3/\text{MnIn}_2\text{S}_4/\text{PVDF/NF}$  and  $\text{In}_2\text{S}_3/\text{MnIn}_2\text{S}_4/\text{NF}$ ; (d) the proposed enhancement mechanism of  $\text{H}_2\text{O}_2$  generation; (e) reusability and stability of  $\text{In}_2\text{S}_3/\text{MnIn}_2\text{S}_4/\text{PVDF/NF}$  for four successive tests; (f) the yields of  $\text{H}_2\text{O}_2$  compared  $\text{In}_2\text{S}_3/\text{MnIn}_2\text{S}_4/\text{PVDF/NF}$  with others.

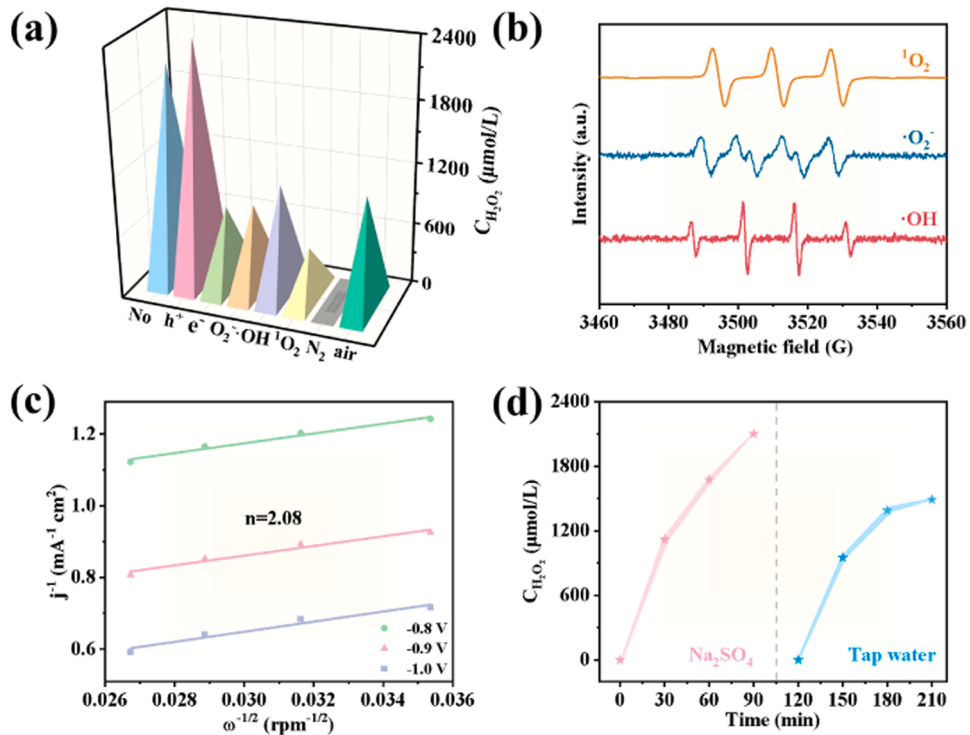
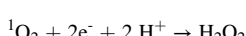
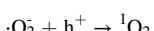


**Fig. 5.** (a) Active radical trapping experiments; (b) EPR signals of TEMP- ${}^1\text{O}_2$ , DMPO- $\cdot\text{O}_2^-$  and DMPO- $\cdot\text{OH}$  obtained with  $\text{In}_2\text{S}_3/\text{MnIn}_2\text{S}_4/\text{PVDF/NF}$  in  $\text{H}_2\text{O}_2$  alone system; (c) Koutecky-Levich plots of the ORR data measured by RDE analysis; (d) effect of electrolyte on  $\text{H}_2\text{O}_2$  production.



The high production of  $\text{H}_2\text{O}_2$  is due to the ingenious design of the photoelectrode material. Owing to the hollow porous tubular structure, abundant active sites and strong coupling S-scheme heterointerface, there are enhanced consequently light absorption, separation efficiency

and high redox capability of photoexcited carriers. The hydrophobic PVDF layer serves as a gas diffusion layer, forming a liquid-solid-gas triphase interface that can quickly transfer O<sub>2</sub> to the In<sub>2</sub>S<sub>3</sub>/MnIn<sub>2</sub>S<sub>4</sub> catalyst layer, at the same time, the hollow structure of In<sub>2</sub>S<sub>3</sub>/MnIn<sub>2</sub>S<sub>4</sub> can also promote oxygen mass transfer, greatly increasing the oxygen concentration on the catalyst surface, thereby minimizing electron-hole recombination and maximizing the H<sub>2</sub>O<sub>2</sub> yield.

The presently used PEC systems for H<sub>2</sub>O<sub>2</sub> production usually need high concentrations of electrolytes. Therefore, it is imperative to investigate the feasibility of using tap water as the electrolyte due to the difficulty of separating H<sub>2</sub>O<sub>2</sub> from electrolytes. Moreover, an additional process to purify the as-synthesized H<sub>2</sub>O<sub>2</sub> from tap water in the PEC cell is needed. Notably, the average concentration of H<sub>2</sub>O<sub>2</sub> in tap water for In<sub>2</sub>S<sub>3</sub>/MnIn<sub>2</sub>S<sub>4</sub>/PVDF/NF was 1.49 mmol/L (Fig. 5d), much higher than the required concentration for Fenton reaction. As shown in Fig. S10a, using the saturated vapor pressure difference between H<sub>2</sub>O and H<sub>2</sub>O<sub>2</sub>, a synthesis-concentration tandem system was designed for high concentration H<sub>2</sub>O<sub>2</sub> production. Low concentration H<sub>2</sub>O<sub>2</sub> solution (about 1.5 mmol/L) was firstly synthesized, and then high concentration H<sub>2</sub>O<sub>2</sub> solution (about 5.1 mmol/L) was obtained by vacuum oven. Through vacuum concentration, the concentration of H<sub>2</sub>O<sub>2</sub> solution increased by about 3.4 times with little H<sub>2</sub>O<sub>2</sub> loss (Fig. S10b).

### 3.3. In Situ HClO production on photoanode

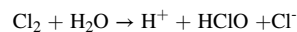
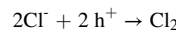
The Cl<sup>-</sup> oxidation reaction (ClOR) over In<sub>2</sub>S<sub>3</sub>/MnIn<sub>2</sub>S<sub>4</sub>/CP photoanode in 35 g/L NaCl electrolyte (pH = 5.6) was evaluated in a three-electrode system. The LSV curves were obtained from the In<sub>2</sub>S<sub>3</sub>/MnIn<sub>2</sub>S<sub>4</sub>/CP in the concentration of Cl<sup>-</sup> range from 0 to 35 g/L (Fig. 6a). The onset potential of In<sub>2</sub>S<sub>3</sub>/MnIn<sub>2</sub>S<sub>4</sub>/CP shifted to a lower potential with increasing Cl<sup>-</sup> concentration and an increased current density in the electrolyte can be observed for ClOR, the low potential (1.3 V<sub>Ag/AgCl</sub>) required for In<sub>2</sub>S<sub>3</sub>/MnIn<sub>2</sub>S<sub>4</sub>/CP to realize a current density of

5 mA cm<sup>-2</sup> in with 35 g/L Cl<sup>-</sup> oxidation. As shown in Fig. S11a-b, the LSV of In<sub>2</sub>S<sub>3</sub>/MnIn<sub>2</sub>S<sub>4</sub>/CP and Pt anode and the EC and PEC LSV curves in 35 g/L NaCl electrolyte indicated that the ClOR on In<sub>2</sub>S<sub>3</sub>/MnIn<sub>2</sub>S<sub>4</sub>/CP is photoelectric synergistic catalysis.

The experimental conditions were optimized (Fig. 6b), and a high HClO production of 28.5 mg/L was achieved at a voltage of 1.3 V<sub>Ag/AgCl</sub> within 1.5 h. To investigate the cycling stability of the In<sub>2</sub>S<sub>3</sub>/MnIn<sub>2</sub>S<sub>4</sub>/CP electrode, HClO production was tested by four cycles (Fig. 6c). The HClO yield was maintained at ~95% of the initial test and the FE (%) could be maintained at over 50%, demonstrating a satisfactory reusability.

Then the applicability of In<sub>2</sub>S<sub>3</sub>/MnIn<sub>2</sub>S<sub>4</sub>/CP for HClO production with natural seawater (Bohai Sea, China) was also evaluated (Fig. S12). Even in natural seawater, In<sub>2</sub>S<sub>3</sub>/MnIn<sub>2</sub>S<sub>4</sub>/CP delivered an impressive HClO yield of 36.9 mg/L within 2 h.

For insights into the mechanism of in situ produced HClO, the results of active radical trapping experiment were derived (Fig. 6d). The results indicated that h<sup>+</sup> is the key active group due to the significant reduction in the HClO production by adding ammonium oxalate. To demonstrate this conjecture, e<sup>-</sup> capture agent (potassium persulfate) was used and found that the yield of HClO increased, which was because more h<sup>+</sup> was involved in the ClOR reaction. The improved oxidation performance by the In<sub>2</sub>S<sub>3</sub>/MnIn<sub>2</sub>S<sub>4</sub>/CP could be attributed to the enhanced separation of e<sup>-</sup> and h<sup>+</sup> in the S-scheme heterojunction driven by visible light, and h<sup>+</sup> oxidized to form HClO assisted by the effect of applied electric field [35]. Combined with previous analysis (Fig. S11b-c), the ClOR on In<sub>2</sub>S<sub>3</sub>/MnIn<sub>2</sub>S<sub>4</sub>/CP was photoelectric synergistic catalysis.



HClO as a popular chemical could be used in many fields such as bleaching and waste treatment. With rhodamine B (RhB), methyl orange

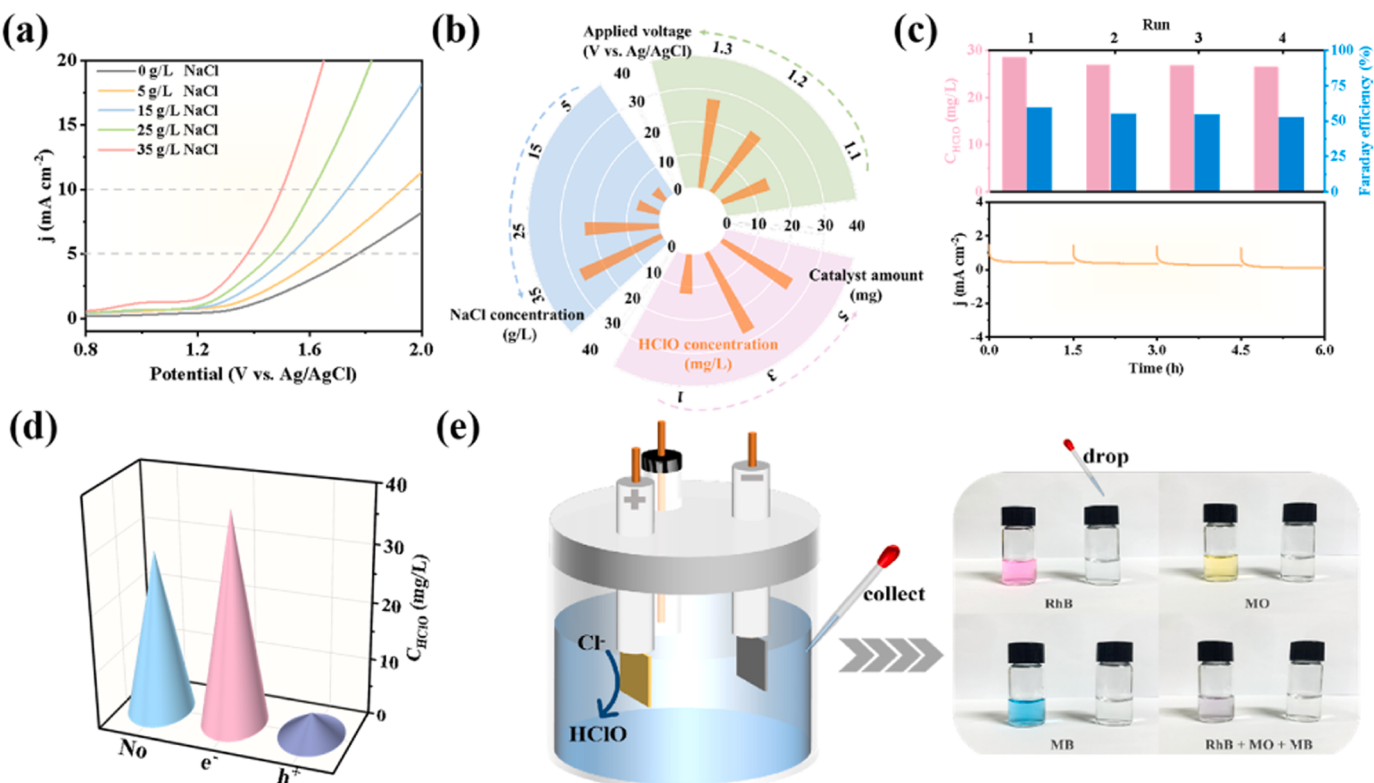


**Fig. 6.** (a) LSV curves of In<sub>2</sub>S<sub>3</sub>/MnIn<sub>2</sub>S<sub>4</sub>/CP electrode in different concentrations of NaCl solution ranges from 0 to 35 g/L; (b) the comparisons of HClO yield under various NaCl concentration, applied voltage and catalyst amount; (c) cycle runs of In<sub>2</sub>S<sub>3</sub>/MnIn<sub>2</sub>S<sub>4</sub>/CP for ClOR at 1.3 V<sub>Ag/AgCl</sub>; (d) influence of different scavengers for HClO production; (e) dyes (5 ppm) bleaching effect of the produced HClO solution (right).

(MO), methylene blue (MB) and their mixed solutions as models, the bleaching and waste treatment performance of HClO were studied. As shown in Fig. 6e, the bleaching effect of the produced HClO was remarkable. Similarly, the RhB-dyed facecloth was also bleached to white rapidly in the produced HClO solution within 30 s (Fig. S13 and Movie S1). It indicated that the HClO was a highly effective bleaching agent and oxidant with practical applications. The excellent bleaching effect was due to the formed HClO was able to destroy the dye and its colored by-products, making it efficient for decolorization.

Furthermore, radical quenching experiment was conducted to explore the degradation mechanism of dye. For anodic HClO degradation process, the furfuryl alcohol (FA) and isopropyl alcohol (IPA) were used as the  $^1\text{O}_2$  and  $\cdot\text{OH}$  quencher, respectively, it was found that the degradation of MB was inhibited (Fig. S14), indicating that  $^1\text{O}_2$  and  $\cdot\text{OH}$  as the reactive species can rapidly degrade MB at the anode [36,37].

### 3.4. In situ simultaneous production of $\text{H}_2\text{O}_2$ and HClO in H-type cell

An asymmetric hybrid electrolyzer was established coupling efficient

ORR on  $\text{In}_2\text{S}_3/\text{MnIn}_2\text{S}_4/\text{PVDF}/\text{NF}$  photocathode for  $\text{H}_2\text{O}_2$  production in 0.1 M  $\text{Na}_2\text{SO}_4$  ( $\text{pH}=3$ ) and ClOR on  $\text{In}_2\text{S}_3/\text{MnIn}_2\text{S}_4/\text{CP}$  photoanode for HClO production in 35 g/L  $\text{NaCl}$  ( $\text{pH}=5.6$ ) in an H-type cell (Fig. 7a). Compared with the PEC ORR||OER system, the PEC ORR||ClOR electrolysis required lower potentials of 1.56 V to reach the current densities of  $10 \text{ mA cm}^{-2}$ , which was 270 mV lower than that in the ORR||OER system, demonstrating the energy saving advantage of replacing OER with ClOR (Fig. 7b). As displayed in Fig. 7c, the accumulation concentration of  $\text{H}_2\text{O}_2$  and HClO could reach 1.49 mmol/L and 17.3 mg/L at 1.2 V<sub>Ag/AgCl</sub> within 2 h, and satisfactory yields of both were obtained. The stable cell voltage and negligible decrease in current density revealed that both  $\text{In}_2\text{S}_3/\text{MnIn}_2\text{S}_4/\text{PVDF}/\text{NF}$  and  $\text{In}_2\text{S}_3/\text{MnIn}_2\text{S}_4/\text{CP}$  exhibited satisfactory stability, which is a key index for assessing the practical applications of photoelectrodes. The electrolyser coupling the two reactions has an excellent yield for  $\text{H}_2\text{O}_2$  and HClO, and the stability of photoelectrolysis could achieve to 8 h (refreshing of the electrolyte every 2 h, Fig. 7d).

Besides, a self-powered PEC system was designed, which is equipped with solar panel ( $\sim 1.5$  V) to provide constant voltage (Fig. 7e), and

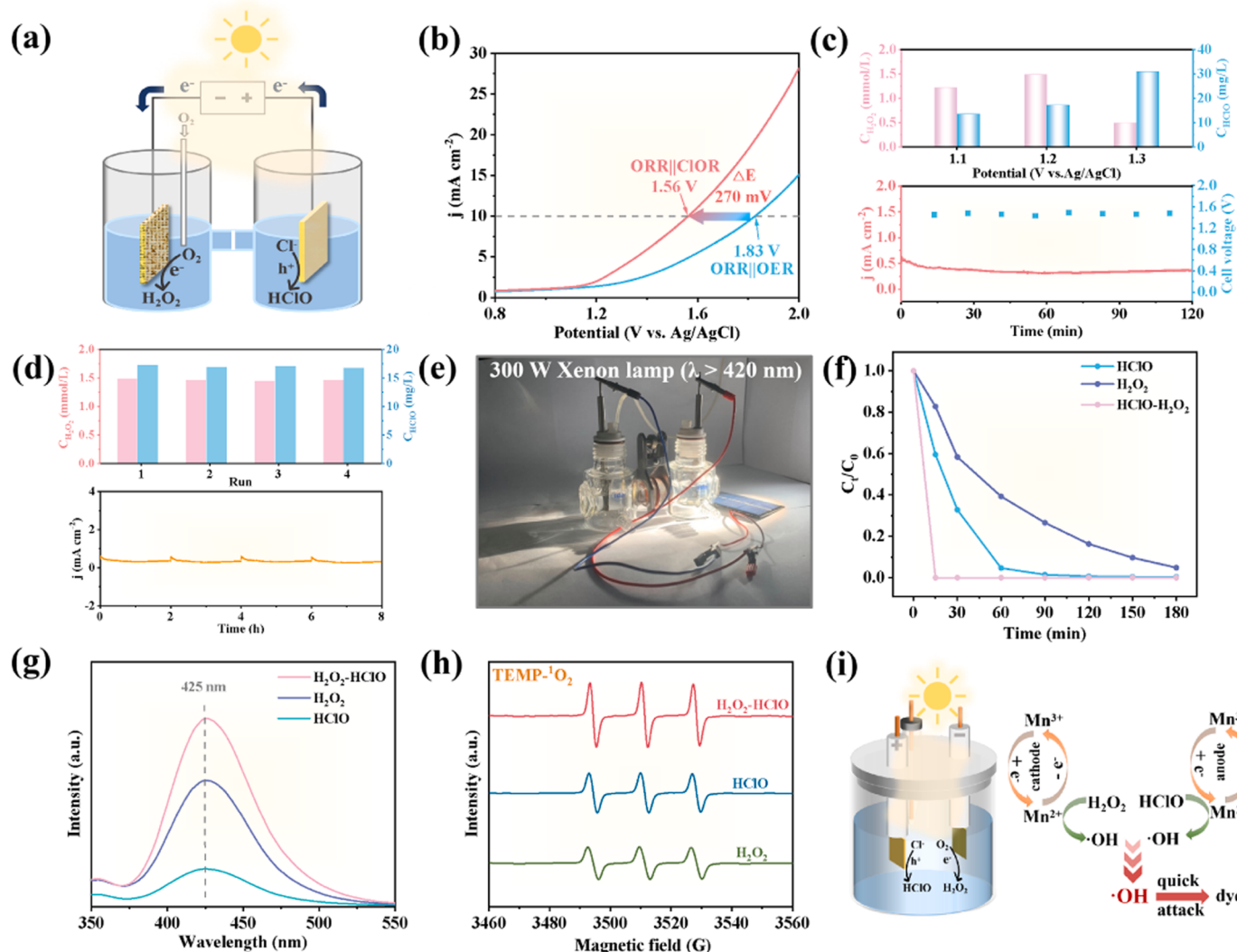
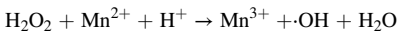
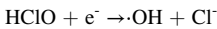
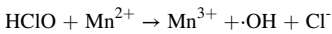


**Fig. 7.** (a) Schematic diagram of  $\text{H}_2\text{O}_2$  and HClO were produced simultaneously at the cathode and anode; (b) LSV plots of the ORR||ClOR and ORR||OER systems by  $\text{In}_2\text{S}_3/\text{MnIn}_2\text{S}_4/\text{PVDF}/\text{NF}||\text{In}_2\text{S}_3/\text{MnIn}_2\text{S}_4/\text{CP}$ ; (c) the effect of bias potentials on the generation of  $\text{H}_2\text{O}_2$  and HClO and current density and cell voltage versus time curves of this PEC cascade production system at 1.2 V<sub>Ag/AgCl</sub>; (d) recyclability and stability of the ORR||ClOR system; (e) optical image of the self-powered PEC system; (f) degradation efficiency of MB in  $\text{H}_2\text{O}_2$  alone system (at  $-0.6 \text{ V}_{\text{Ag/AgCl}}$ ), HClO alone system (at  $1.3 \text{ V}_{\text{Ag/AgCl}}$ ),  $\text{H}_2\text{O}_2$ -HClO coupling system (at  $1.3 \text{ V}_{\text{Ag/AgCl}}$ ); (g) fluorescence study for  $\cdot\text{OH}$  radical trapping experiment of the HClO alone system and  $\text{H}_2\text{O}_2$ -HClO coupling system; (h) EPR signals of TEMP-<sup>1</sup>O<sub>2</sub> obtained with  $\text{H}_2\text{O}_2$ , HClO alone system and  $\text{H}_2\text{O}_2$ -HClO coupling system; (i) proposed mechanism of  $\text{H}_2\text{O}_2$ /HClO activation to  $\cdot\text{OH}$  for enhanced degradation organic pollutants.

successfully produced 461  $\mu\text{mol/L}$  of  $\text{H}_2\text{O}_2$  and 3.68 mg/L of  $\text{HClO}$ , further demonstrating the potential of the designed PEC cell to produce  $\text{H}_2\text{O}_2$  and  $\text{HClO}$  for upgraded remodeling.

Furthermore, the degradation performance of  $\text{H}_2\text{O}_2$ ,  $\text{HClO}$  alone systems and  $\text{H}_2\text{O}_2\text{-HClO}$  coupling system were investigated by using  $\text{In}_2\text{S}_3/\text{MnIn}_2\text{S}_4/\text{PVDF/NF}$  photocathode and  $\text{In}_2\text{S}_3/\text{MnIn}_2\text{S}_4/\text{CP}$  photoanode in a single-chamber cell. As shown in Fig. 7f, in the  $\text{H}_2\text{O}_2\text{-HClO}$  coupling system ( $\text{pH} = 3.0$ ), MB at a concentration of 10 ppm was completely degraded by 20 min. Conversely, the degradation efficiency of MB in the  $\text{HClO}$  or  $\text{H}_2\text{O}_2$  alone systems was 98.5% or 95.1% after 90 min or 180 min, respectively. The results of MB degradation demonstrated that the  $\text{H}_2\text{O}_2\text{-HClO}$  coupling system has a stronger degradation ability.

To explore the mechanism of enhanced degradation performance of  $\text{H}_2\text{O}_2\text{-HClO}$  coupling system, the  $\cdot\text{OH}$  was confirmed by PL spectrometry using terephthalic acid (TA) as a probe (Fig. 7g), the stronger fluorescence intensity of  $\text{H}_2\text{O}_2\text{-HClO}$  coupling system indicated that the concentration of  $\cdot\text{OH}$  was higher compared to than  $\text{HClO}$  and  $\text{H}_2\text{O}_2$  alone systems, achieving a "1 + 1 > 2" effect. As shown in Fig. S15, the role of  $\cdot\text{OH}$  was also confirmed by the scavenging experiment using isopropyl alcohol (IPA) as a common  $\cdot\text{OH}$  scavenger. The results indicated that the synergistic effect of co-produced  $\text{H}_2\text{O}_2$  and  $\text{HClO}$  presented to generate more  $\cdot\text{OH}$  by activation of  $\text{HClO}$  and  $\text{H}_2\text{O}_2$  at electrode, resulting high-efficiency degradation of MB in a single-chamber cell. According to the XPS analysis (Fig. S16), the  $\text{Mn}^{2+}/\text{Mn}^{3+}$  redox pairs may play an important role in the Fenton-like degradation of MB. Until now, the enhanced Fenton-like degradation mechanism of the  $\text{H}_2\text{O}_2\text{-HClO}$  coupling system could be proposed (see Fig. 7i).



The  $\text{In}_2\text{S}_3/\text{MnIn}_2\text{S}_4/\text{PVDF/NF}$  photocathode can produce  $\text{H}_2\text{O}_2$  and  $\text{In}_2\text{S}_3/\text{MnIn}_2\text{S}_4/\text{CP}$  photoanode can produce  $\text{HClO}$ , the synergistic effect of co-produced  $\text{H}_2\text{O}_2$  and  $\text{HClO}$  presented to generate more  $\cdot\text{OH}$  by activation of  $\text{HClO}$  and  $\text{H}_2\text{O}_2$  at electrode, resulting high-efficiency degradation of MB.

The TEMP- $^1\text{O}_2$  signals were further identified by EPR spin-trapping experiments, which confirmed the existence of  $^1\text{O}_2$ . As shown in Fig. 7h, the increase of peak intensity showed that the  $^1\text{O}_2$  content increased in the  $\text{H}_2\text{O}_2\text{-HClO}$  coupling system, which indicated that more  $^1\text{O}_2$  was produced. Therefore, it was confirmed that the reaction ( $\text{H}_2\text{O}_2 + \text{HClO} \rightarrow \text{H}^+ + \text{Cl}^- + \text{H}_2\text{O} + ^1\text{O}_2$ ) occurred, thus decreased the MB concentration (Fig. S17).

The stability and reusability of the  $\text{H}_2\text{O}_2\text{-HClO}$  coupling system were investigated by the cycle degradation of MB on the same electrode. As shown in Fig. S18, the five cycles of MB-degradation experiment proceeded, and the MB removal still achieved 100% after five cycles.

#### 4. Conclusion

In this study, bifunctional S-scheme  $\text{In}_2\text{S}_3/\text{MnIn}_2\text{S}_4$  photoelectrocatalyst was fabricated by ion exchange. Due to the hollow tubular structures and hydrophobic PVDF layer can improve the  $\text{O}_2$  mass transfer and reduce the decomposition of  $\text{H}_2\text{O}_2$ , the  $\text{H}_2\text{O}_2$  yield obtained by  $\text{In}_2\text{S}_3/\text{MnIn}_2\text{S}_4/\text{PVDF/NF}$  photocathode achieved 2108  $\mu\text{mol/L}$ . Meanwhile, the  $\text{In}_2\text{S}_3/\text{MnIn}_2\text{S}_4/\text{CP}$  photoanode had a stronger oxidation activity toward  $\text{Cl}^-$  to generate a relatively high concentration of  $\text{HClO}$  (28.5 mg/L). Besides, an energy-saving co-photoelectrocatalysis was achieved by coupling the  $\text{O}_2$  reduction reaction (ORR) with  $\text{Cl}^-$  oxidation reaction (ClOR) using  $\text{In}_2\text{S}_3/\text{MnIn}_2\text{S}_4/\text{PVDF/NF}$  photocathode and  $\text{In}_2\text{S}_3/\text{MnIn}_2\text{S}_4/\text{CP}$  photoanode, in-situ simultaneous produce  $\text{H}_2\text{O}_2$  and

$\text{HClO}$ . The voltage of ORR||ClOR was 270 mV less than that of ORR||OER, and the assembled electrolyser has a low voltage of 1.2 V<sub>Ag/AgCl</sub> to drive the two half reactions. In addition, taking advantage of the synergistic effect of  $\text{H}_2\text{O}_2$  and  $\text{HClO}$  produced in-situ, more  $\cdot\text{OH}$  was produced by Fenton-like reaction, which realizes the rapid degradation of MB. Additionally,  $^1\text{O}_2$  also contributed to the degradation of dyes. The mechanisms of  $\text{H}_2\text{O}_2\text{-HClO}$  production and synergistic degradation were discussed. This study provided guidance for the preparation of high-activity bifunctional catalyst and photoelectrodes for the coupling ORR with ClOR as well the synergistic treatment of pollutants by  $\text{H}_2\text{O}_2$  and  $\text{HClO}$ .

#### CRediT authorship contribution statement

Chen Yaoyue: Writing – review & editing, Writing – original draft.  
Zhang Lei: Writing – review & editing, Writing – original draft.

#### Declaration of Competing Interest

The authors declare that they have no known competing financial interests or personal relationships that could have appeared to influence the work reported in this paper.

#### Data Availability

Data will be made available on request.

#### Acknowledgements

This project was supported by National Natural Science Foundation of China (NSFC 52072164) and (NSFC 52102104), Liaoning Revitalization Talents Program (No. XLYC1902066). The authors also thank to Weiliang Huang from Shiyanjia Lab ([www.shiyanjia.com](http://www.shiyanjia.com)) for the TEM analysis in this study.

#### Conflicts of interest

There are no conflicts of interest to declare.

#### Appendix A. Supporting information

Supplementary data associated with this article can be found in the online version at [doi:10.1016/j.apcatb.2024.123768](https://doi.org/10.1016/j.apcatb.2024.123768).

#### References

- [1] K. Zhang, M. Dan, J. Yang, F. Wu, L. Wang, H. Tang, Z. Liu, Surface energy mediated sulfur vacancy of  $\text{ZnIn}_2\text{S}_4$  atomic layers for photocatalytic  $\text{H}_2\text{O}_2$  production, *Adv. Funct. Mater.* 33 (2023) 2302964, <https://doi.org/10.1002/adfm.202302964>.
- [2] Y. Shi, H. Shou, H. Li, G. Zhan, X. Liu, Z. Yang, C. Mao, J. Cheng, X. Zhang, Y. Jiang, S. Zhao, J. Wang, X. Liu, L. Song, H. Sun, Li Zhang, Visible light-driven conversion of carbon-sequestered seawater into stoichiometric CO and  $\text{HClO}$  with nitrogen-doped  $\text{BiOCl}$  atomic layers, *Angew. Chem. Int. Ed.* 62 (2023) e202302286, <https://doi.org/10.1002/anie.202302286>.
- [3] H. Wu, T. He, M. Dan, L. Du, N. Li, Z. Liu, Activated Ni-based metal-organic framework catalyst with well-defined structure for electrosynthesis of hydrogenperoxide, *Chem. Eng. J.* 435 (2022) 134863, <https://doi.org/10.1016/j.cej.2022.134863>.
- [4] R. Pang, Y. Miseki, S. Okunaka, K. Sayama, Photocatalytic production of hypochlorous acid over  $\text{Pt}/\text{WO}_3$  under simulated solar light, *ACS Sustain. Chem. Eng.* 8 (2020) 8629–8637, <https://doi.org/10.1021/acssuschemeng.0c01341>.
- [5] X. Liu, A. Ren, A. Liu, X. Jiang, L. Zhang, Simultaneous photocatalytic tetracycline oxidation and Cr(VI) reduction by a 0D/3D hierarchical  $\text{Bi}_2\text{WO}_6@\text{CoO}$  Z-scheme heterostructure: in situ interfacial engineering and charge regulation mechanism, *J. Environ. Manag.* 342 (2023) 118134, <https://doi.org/10.1016/j.jenvman.2023.118134>.
- [6] J. Wei, D. Yuan, X. Wu, Enabling direct  $\text{H}_2\text{O}_2$  electrosynthesis of 100% selectivity at 100 mA  $\text{cm}^{-2}$  using a continuous flow sulfite/air fuel cell, *Chem. Eng. J.* 455 (2023) 140695, <https://doi.org/10.1016/j.cej.2022.140695>.
- [7] L. Ding, J. Zhao, Z. Bao, S. Zhang, H. Shi, J. Liu, G. Wang, X. Peng, X. Zhong, J. Wang, Synchronous generation of green oxidants  $\text{H}_2\text{O}_2$  and  $\text{O}_3$  by using a

heterojunction bifunctional ZnO/ZnS@C electrocatalyst, *J. Mater. Chem. A* 11 (2023) 3454–3463, <https://doi.org/10.1039/D2TA09450A>.

[8] L. Zhang, Z. Wang, J. Qiu, Energy-saving hydrogen production by seawater electrolysis coupling sulfion degradation, *Adv. Mater.* 34 (2022) 2109321, <https://doi.org/10.1002/adma.202109321>.

[9] Z. Zhang, X. Li, C. Zhong, N. Zhao, Y. Deng, X. Han, W. Hu, Spontaneous synthesis of silver-nanoparticle-decorated transition-metal hydroxides for enhanced oxygen evolution reaction, *Angew. Chem. Int. Ed.* 59 (2020) 7245, <https://doi.org/10.1002/anie.202001703>.

[10] F. Sun, J. Qin, Z. Wang, M. Yu, X. Wu, X. Sun, J. Qiu, Energy-saving hydrogen production by chlorine-free hybrid seawater splitting coupling hydrazine degradation, *Nat. Commun.* 12 (2021) 4182, <https://doi.org/10.1038/s41467-021-24529-3>.

[11] L. Zhang, Y. Li, M. Wang, H. Liu, H. Chen, Y. Cai, T. Li, M. Xu, S. Bao, The construction of ZnS-In<sub>2</sub>S<sub>3</sub> nanonests and their heterojunction boosted visible-light photocatalytic/photoelectrocatalytic performance, *N. J. Chem.* 43 (2019) 14402–14408, <https://doi.org/10.1039/C9NJ02984B>.

[12] P. Wu, H. Yelemulati, S. Zhu, B. Peng, H. Li, H. Ye, J. Hou, K. Wu, Z. Liu, Amorphous-crystalline junction oxygen vacancy-enriched CoPi/ZnIn<sub>2</sub>S<sub>4</sub>/a-B-TiO<sub>2</sub> catalyst for oxygen evolution reaction, *Chem. Eng. J.* 466 (2023) 143252, <https://doi.org/10.1016/j.cej.2023.143252>.

[13] M. Zhang, Y. Zhang, L. Ye, Z. Yu, R. Liu, Y. Qiao, L. Sun, J. Cui, X. Lu, In situ fabrication Ti<sub>3</sub>C<sub>2</sub>F<sub>x</sub> MXene/CdIn<sub>2</sub>S<sub>4</sub> Schottky junction for photocatalytic oxidation of HMF to DFF under visible light, *Appl. Catal. B: Environ.* 330 (2023) 122635, <https://doi.org/10.1016/j.apcatb.2023.122635>.

[14] F. Chen, Y. Li, M. Zhou, X. Gong, Y. Gao, G. Cheng, S. Ren, D. Han, Smart multifunctional direct Z-scheme In<sub>2</sub>S<sub>3</sub>@PCN-224 heterojunction for simultaneous detection and photodegradation towards antibiotic pollutants, *Appl. Catal. B: Environ.* 328 (2023) 122517, <https://doi.org/10.1016/j.apcatb.2023.122517>.

[15] H. Zeng, S. Ai, Y. Chai, R. Yuan, H. Liu, Defect engineering of In<sub>2</sub>S<sub>3</sub> nanoflowers through tungsten doping for ultrasensitive visible-light-excited photoelectrochemical sensors, *J. Mater. Chem. C* 9 (2021) 7384–7391, <https://doi.org/10.1039/DITC01491>.

[16] Y. Xiong, L. Yang, Y. Zhu, Q. Lai, P. Li, P. Xiao, G. Cao, Tuning electronic structure of 2D In<sub>2</sub>S<sub>3</sub> via P doping and size controlling toward efficient photoelectrochemical water oxidation, *Sol. RRL* 5 (2021) 200618, <https://doi.org/10.1002/solr.202000618>.

[17] X. Han, B. Lu, X. Huang, C. Liu, S. Chen, J. Chen, Z. Zeng, S. Deng, J. Wang, Novel p- and n-type S-scheme heterojunction photocatalyst for boosted CO<sub>2</sub> photoreduction activity, *Appl. Catal. B: Environ.* 316 (2022) 121587, <https://doi.org/10.1016/j.apcatb.2022.121587>.

[18] X. Liu, Z. Yang, L. Zhang, In-situ fabrication of 3D hierarchical flower-like β-Bi<sub>2</sub>O<sub>3</sub>@CoO Z-scheme heterojunction for visible-driven simultaneous degradation of multi-pollutants, *J. Hazard. Mater.* 403 (2021) 123566, <https://doi.org/10.1016/j.jhazmat.2020.123566>.

[19] J. Xiong, H. Li, J. Zhou, J. Di, Recent progress of indium-based photocatalysts: classification, regulation and diversified applications, *Coord. Chem. Rev.* 473 (2022) 214819, <https://doi.org/10.1016/j.ccr.2022.214819>.

[20] Z. Chen, H. Chen, K. Wang, J. Chen, M. Li, Y. Wang, P. Tsakararas, S. Song, Enhanced TiO<sub>2</sub> photocatalytic 2e<sup>-</sup> oxygen reduction reaction via interfacial microenvironment regulation and mechanism analysis, *ACS Catal.* 13 (2023) 6497–6508, <https://doi.org/10.1021/acscatal.3c00994>.

[21] M. Ou, M. Geng, X. Fang, W. Shao, F. Bai, S. Wan, C. Ye, Y. Wu, Y. Chen, Tailored BiVO<sub>4</sub> photoanode hydrophobic microenvironment enables water oxidative H<sub>2</sub>O<sub>2</sub> accumulation, *Adv. Sci.* 10 (2023) 2300169, <https://doi.org/10.1002/advs.202300169>.

[22] H. Wang, J. Zhang, D. Wang, Z. Wang, Y. Chen, X. Feng, Flexible triphase enzyme electrode based on hydrophobic porous PVDF membrane for high-performance bioassays, *Biosens. Bioelectron.* 183 (2021) 113201, <https://doi.org/10.1016/j.bios.2021.113201>.

[23] Y. Zhao, S. Hojabri, S. Sarrouf, A.N. Alshawabkeh, Electrogeneration of H<sub>2</sub>O<sub>2</sub> by graphite felt double coated with polytetrafluoroethylene and polydimethylsiloxane, *J. Environ. Chem. Eng.* 10 (2022) 108024, <https://doi.org/10.1016/j.jece.2022.108024>.

[24] Q. Chen, X. Wang, W. Liu, T. Luo, Z. Jin, Y. Zhang, J. Huang, H. Zhang, J. Wang, F. Peng, Rapid photocatalytic reduction of Cr(VI) with high concentration in wastewater by In<sub>2</sub>S<sub>3</sub>-ZnIn<sub>2</sub>S<sub>4</sub> nanocomposite under visible light, *J. Solid. State Chem.* 306 (2022) 122721, <https://doi.org/10.1016/j.jssc.2021.122721>.

[25] Y. Pi, S. Jin, X. Li, S. Tu, Z. Li, J. Xiao, Encapsulated MWCNT@MOF-derived In<sub>2</sub>S<sub>3</sub> tubular heterostructures for boosted visible-light-driven degradation of tetracycline, *Appl. Catal. B: Environ.* 256 (2019) 117882, <https://doi.org/10.1016/j.apcatb.2019.117882>.

[26] H. Liu, X. Ma, Y. Rao, Y. Liu, J. Liu, L. Wang, M. Wu, Heteromorphic NiCo<sub>2</sub>S<sub>4</sub>/Ni<sub>3</sub>S<sub>2</sub>/Ni foam as a self-standing electrode for hydrogen evolution reaction in alkaline solution, *ACS Appl. Mater. Interfaces* 10 (2018) 10890–10897, <https://doi.org/10.10121.acsmi.8b00296>.

[27] L. Yang, Y. Hu, L. Zhang, Architecting Z-scheme Bi<sub>2</sub>S<sub>3</sub>@CoO with 3D chrysanthemums-like architecture for both photoelectro-oxidation and -reduction performances under visible light, *Chem. Eng. J.* 378 (2019) 122092, <https://doi.org/10.1016/j.cej.2019.122092>.

[28] Y. Wang, Y. Liu, F. Tian, S. Bao, C. Sun, W. Yang, Y. Yu, MnIn<sub>2</sub>S<sub>4</sub> nanosheets growing on rods-like β-MnO<sub>2</sub> via covalent bonds as high-performance photocatalyst for boosting Cr(VI) photocatalytic reduction under visible light irradiation: Behavior and mechanism study, *J. Colloid Interface Sci.* 625 (2022) 264–277, <https://doi.org/10.1016/j.jcis.2022.06.015>.

[29] Y. Wang, Y. Tang, J. Sun, X. Wu, H. Liang, Y. Qu, L. Jing, BiFeO<sub>3</sub>/Bi<sub>2</sub>Fe<sub>4</sub>O<sub>9</sub> S-scheme heterojunction hollow nanospheres for high-efficiency photocatalytic o-chlorophenol degradation, *Appl. Catal. B: Environ.* 319 (2022) 121893, <https://doi.org/10.1016/j.apcatb.2022.121893>.

[30] Q. Li, L. Wang, J. Song, L. Zhang, C. Shao, H. Li, H. Zhang, Facile synthesis of hierarchical S-scheme In<sub>2</sub>S<sub>3</sub>/Bi<sub>2</sub>WO<sub>6</sub> heterostructures with enhanced photocatalytic activity, *J. Environ. Chem. Eng.* 11 (2023) 109832, <https://doi.org/10.1016/j.jece.2023.109832>.

[31] H. Huang, Q. Zhang, R. Shi, C. Su, Y. Wang, J. Zhao, T. Zhang, Synergistic effect of triphase interface and fluid control for efficient photosynthesis of residue-free H<sub>2</sub>O<sub>2</sub>, *Appl. Catal. B: Environ.* 317 (2022) 121731, <https://doi.org/10.1016/j.apcatb.2022.121731>.

[32] L. Qiao, J. Bai, T. Luo, J. Lia, Y. Zhang, L. Xia, T. Zhou, Q. Xu, B. Zhou, High yield of H<sub>2</sub>O<sub>2</sub> and efficient S recovery from toxic H<sub>2</sub>S splitting through a self-driven photoelectrocatalytic system with a microporous GDE cathode, *Appl. Catal. B: Environ.* 238 (2018) 491–497, <https://doi.org/10.1016/j.apcatb.2018.07.051>.

[33] X. Mei, J. Bai, S. Chen, M. Zhou, H. Zhou, P. Jiang, C. Zhou, F. Fang, Y. Zhang, J. Li, M. Long, B. Zhou, Efficient SO<sub>2</sub> removal and highly synergistic H<sub>2</sub>O<sub>2</sub> production based on a novel dual-function photoelectrocatalytic system, *Environ. Sci. Technol.* 54 (2020) 11515–11525, <https://doi.org/10.1021/acs.est.0c00886>.

[34] P. Cao, X. Quan, K. Zhao, X. Zhao, S. Chen, H. Yu, Durable and selective electrochemical H<sub>2</sub>O<sub>2</sub> synthesis under a large current enabled by the cathode with highly hydrophobic three-phase architecture, *ACS Catal.* 11 (2021) 13797–13808, <https://doi.org/10.1021/acscatal.1c03236>.

[35] A. Tolosana-Moranchel, S. McMichael, J.W.J. Hamilton, J.A. Byrne, P. Fernandez-Ibanez, Electrochemically assisted photocatalytic degradation of contaminants of emerging concern in simulated wastewater using WO<sub>3</sub>- elucidation of mechanisms, *Chem. Eng. J.* 458 (2023) 141442, <https://doi.org/10.1016/j.cej.2023.141442>.

[36] D. Fu, Y. Zhu, T. Yu, J. Li, L. Chen, Y. Cui, Z. Liu, H. Wang, In-situ efficient electrosynthesis of H<sub>2</sub>O<sub>2</sub>-NaClO based on the media pH and catalyst mutual selection mechanism, *J. Power Sources* 553 (2023) 232306, <https://doi.org/10.1016/j.jpowsour.2022.232306>.

[37] M.F. Murrieta, E. Brillas, J.L. Nava, I. Sirés, Photo-assisted electrochemical production of HClO and Fe<sup>2+</sup> as Fenton-like reagents in chloride media for sulfamethoxazole degradation, *Sep. Purif. Technol.* 250 (2020) 117236, <https://doi.org/10.1016/j.seppur.2020.117236>.